Article

Numerical Simulation of Tailings Flow from Dam Failure over Complex Terrain

Yi Yang [1,2], **Xiaowen Zhou** [1,2], **Xiaoyu Chen** [1] **and Chao Xie** [3,*]

1   School of Civil Engineering and Transportation, South China University of Technology, Guangzhou 510641, China; msyangyi@mail.scut.edu.cn (Y.Y.); xwzhou@scut.edu.cn (X.Z.); xiaoyuchen0317@163.com (X.C.)
2   State Key Laboratory of Subtropical Building Science, South China University of Technology, Guangzhou 510641, China
3   School of Architecture and Urban Planning, Guangdong University of Technology, Guangzhou 510090, China
*   Correspondence: xiec61@gdut.edu.cn

Abstract: A tailings dam failure can lead to disastrous impacts on people's livelihood and the surrounding ecological environment. Due to interactions among water, tailings and ground, the mechanism of a tailings flow is more complicated than that of a flood flow. In this paper, the tailings flow is regarded as a homogeneous and incompressible non-Newtonian fluid. Its rheological properties were studied through rheological tests conforming to the Bingham model. The rheological parameters were further used in a Computational Fluid Dynamics (CFD) simulation over complex terrain to explore the tailings flow characteristics. The method was validated with experimental results of a non-Newtonian dam-break flow from literature. The flow characteristics, including flow velocity, runout distance, inundation area and depth, were analyzed in the case of the Dagangding tailings dam. The results showed that the downstream railway and village would not be affected in a conservative scenario. Finally, the effects of two measures for preventing tailings flow hazards were discussed. Setting the check dam and planting grasses and trees can effectively mitigate the damage of tailings flow.

Keywords: tailings dam failure; Bingham model; CFD; inundation area and depth; protection and control measures

1. Introduction

A tailings dam is a permanent infrastructure constructed by intercepting valleys or enclosing lands to form a tailings pond to store discharged tailings from mines after ore separation [1,2]. Once a tailings dam collapses, the downstream region will be seriously affected by the sudden massive release of tailings. Take, for example, the 2019 Brumadinho breach dam event in Brazil. Almost 1.17×10^7 m^3 tailings were released, covering a distance of about 9 km and an inundation area of approximately 3×10^6 m^2. The tailings flow killed 259 people, and 11 were reported missing [3]. Hundreds of tailings dam failure cases have been recorded worldwide [4–7]. The total number of tailings dams in China ranks first in the world. Over forty accidents occurred from 2005, mainly caused by dam-break [8–10]. Therefore, it is crucial to investigate the characteristics of tailings flow from dam failure for safe production and environmental protection.

The mechanical law of tailings flow is quite complicated, involving multiple interdisciplinary fields, including fluid mechanics, sediment transport and geological hazards [9,11,12]. Although neither systematic theories nor specific guidelines of tailings flow have been established, current research has progressed on the methods of empirical formula, model test and numerical simulation. The empirical formula approach estimates the runout distance by analyzing the relationships among dam parameters, tailings characteristics and topographic features [13–15]. It is a relatively rough and straightforward technique based

on plenty of statistical data. Compared to the empirical formula approach, the model test method has unique advantages on a specific project, where accurate dynamics profiles can be portrayed [16–20]. It has the limitation of reflecting the practical behaviour of tailings flow due to the difficulty in determining the mapping between a field- and model-length scale [21]. Thus, it remains an open issue for the application of these two methods.

The numerical simulation technique appears as an effective tool to investigate dam-break-type flow, resulting from its capability in realistic model characterisation. [22–29]. Two typical numerical methods are widely adopted on the simulation of fluid dynamics, namely, Smoothed Particle Hydrodynamics (SPH) and Computational Fluid Dynamics (CFD). The literature has reported the constitutive model development for either SPH or CFD. For example, Pastor et al. [24] proposed a depth-integrated model to simulate flows caused by the failure of tailings dams. The model is enhanced and applied by Dutto et al. [25] on the simulation of different types of flowslides through the SPH method. Similarly, Babaoglu and Simms [26] also adopted the SPH method, incorporating a 'bi-viscosity' model to simulate the non-Newtonian behaviour. Wang et al. [27,28] extended the method to predict the runout routing from two-dimensional to three-dimensional situations. Even though SPH has popularity in dam-break-flow problems, it has limitations in the accurate description of the free surface, which can cause significant numerical error. In contrast, the CFD method has the advantage of tracking surface locations, especially for challenging boundary conditions. Marsooli and Wu [29] set up a three-dimensional CFD model to simulate dam-break flow, and results indicate the suitability of the CFD method for handling the complicated boundary condition of uneven beds. Both Pirulli et al. [30] and Yu et al. [31] implemented a numerical framework to simulate the motion of rapid flow movements, aiming at practical cases. Nonetheless, fluid rheological properties determination that limits the application of the CFD method in simulating tailings flow remains a key issue.

This study investigated the calibration of the rheological properties from the experiment. Then, the obtained rheological values served as the input parameters in numerical simulation. The tailings flow characteristics, including flow velocity, runout distance, inundation area and depth, were explored, focusing on the 3D complex terrain within a commercial CFD framework (ANSYS-CFX). Furthermore, the effects of measures to prevent tailings flow hazards were discussed.

The main contributions of this study are threefold. (1) The rheological properties of tailings slurry versus the different mass concentrations were investigated. It was found that this kind of slurry, which is composed of lead-zine mine tailings with about two-thirds fine particles (0.075~0.25 mm), conforms to the Bingham model. Furthermore, the results demonstrated a non-linear relationship between the mass concentration and yield shear stress or dynamic viscosity. (2) This study establishes a framework linking the modelling of realistic geological topology features to the description of flow characteristics. The principal components of features, such as sharp turning, varying roughness, and sudden flattening, can be accurately captured by this framework. Correspondingly, the flow characteristics composed of flow velocity, runout distance, inundation area and depth can be elaborated. (3) The effects of measures to preventing tailings flow hazards were investigated. Both setting a check dam and planting trees and grasses can mitigate the damage of tailings flow.

2. Methods

The numerical analysis of tailings flow follows the conservation law of mass and momentum. Since the heat change and transfer are negligible, the energy conservation law is not included. Furthermore, additional turbulence equations should be satisfied for the turbulent conditions caused by dam-break.

2.1. Mathematical Models

The mass conservation equation can be expressed in differential form as:

$$\frac{\partial \rho}{\partial t} + div(\rho \boldsymbol{v}) = 0 \tag{1}$$

$$\rho = \rho_s c + \rho_w (1 - c) \tag{2}$$

where ρ is the mixture density, ρ_s is the solid density, ρ_w is the liquid density, c is the mass concentration of tailings flow and t is the time. The operator *div* means the divergence, and v is the flow velocity vector. The tailings flow is assumed to be homogenous and incompressible, and its mixture density remains uniform and constant along the flow process. Therefore, Equation (1) can be simplified in rectangle coordinates as:

$$\frac{\partial u}{\partial x} + \frac{\partial v}{\partial y} + \frac{\partial w}{\partial z} = 0 \tag{3}$$

Here u, v and w are velocity components in x, y and z directions.

Based on Newton's second law, the momentum conservation equation, also known as Navier–Stokes equation, is derived in rectangle coordinates as:

$$\begin{cases} \rho \frac{Du}{Dt} = \frac{\partial \sigma_{xx}}{\partial x} + \frac{\partial \tau_{yx}}{\partial y} + \frac{\partial \tau_{zx}}{\partial z} + F_x \\ \rho \frac{Dv}{Dt} = \frac{\partial \tau_{xy}}{\partial x} + \frac{\partial \sigma_{yy}}{\partial y} + \frac{\partial \tau_{zy}}{\partial z} + F_y \\ \rho \frac{Dw}{Dt} = \frac{\partial \tau_{xz}}{\partial x} + \frac{\partial \tau_{yz}}{\partial y} + \frac{\partial \sigma_{zz}}{\partial z} + F_z \end{cases} \tag{4}$$

where the symbol $\frac{D}{Dt}$ is the substantial derivation and σ_{xx}, σ_{yy} and σ_{zz} are normal stresses in x, y and z directions. τ with different subscripts represents viscous stress components that depend on the rheological model. F_x, F_y and F_z are the body forces in x, y and z directions.

As the flow caused by dam-break is turbulent [30], the flow characteristics are random and usually portrayed by time average. An additional two-equation turbulent model, which includes the turbulent kinetic energy and the rate of turbulent dissipation transport equations [31], was adopted and written as:

$$\begin{cases} \frac{\partial(\rho k)}{\partial t} + div(\rho \overline{u} k) = div\left[\left(\eta + \frac{\eta_t}{\sigma_k}\right) \cdot grad\ k\right] - \rho \varepsilon + \eta_t P_G \\ \frac{\partial(\rho k)}{\partial t} + div(\rho \overline{u} \varepsilon) = div\left[\left(\eta + \frac{\eta_t}{\sigma_\varepsilon}\right) \cdot grad\ \varepsilon\right] - \rho C_2 \frac{\varepsilon^2}{k} + \eta_t C_1 \frac{\varepsilon}{k} P_G \end{cases} \tag{5}$$

where k is the turbulent kinetic energy, η is the dynamic viscosity, ε is the rate of turbulent dissipation transport and the operator *grad* means the gradient. The local dynamic viscosity η_t and the turbulent kinetic energy generation term P_G can be further expressed as:

$$\begin{cases} \eta_t = \rho C_\mu \frac{k^2}{\varepsilon} \\ P_G = 2\left[\left(\frac{\partial u}{\partial x}\right)^2 + \left(\frac{\partial v}{\partial y}\right)^2 + \left(\frac{\partial w}{\partial z}\right)^2\right] + \left(\frac{\partial u}{\partial y} + \frac{\partial v}{\partial x}\right)^2 + \left(\frac{\partial u}{\partial z} + \frac{\partial w}{\partial x}\right)^2 + \left(\frac{\partial v}{\partial z} + \frac{\partial w}{\partial x}\right)^2 \end{cases} \tag{6}$$

Here σ_k, σ_ε, C_1, C_2 and C_μ are adjustable constants with the value of 1.0, 1.3, 1.44, 1.92 and 0.09, respectively, in the simulation.

The Equations (1)–(6) can be rewritten in a general transport equation as the governing equation of the CFD method under the incompressibility condition. It is expressed as:

$$\frac{\partial \phi}{\partial t} + \frac{\partial(u\phi)}{\partial x} + \frac{\partial(v\phi)}{\partial y} + \frac{\partial(w\phi)}{\partial z} = \frac{\partial}{\partial x}\left(\Gamma \frac{\partial \phi}{\partial x}\right) + \frac{\partial}{\partial y}\left(\Gamma \frac{\partial \phi}{\partial y}\right) + \frac{\partial}{\partial z}\left(\Gamma \frac{\partial \phi}{\partial z}\right) + S_\phi \tag{7}$$

where ϕ is the general variable, Γ is the diffusion coefficient and S_ϕ is the source term. Each Cartesian velocity component (u, v, w) satisfies its own transport equation but is non-linear and strongly coupled through the advective fluxes and pressure forces.

Equation (7) can be solved through the Finite Volume Method (FVM), which is the most commonly used method in fluid engineering [18,19]. The governing equations are discretised into algebraic expressions involving the physical quantities at the center of each control volume. The physical quantities are interpolated onto the faces with second-order accuracy. Preconditioning conjugate gradients (PCGs) and smooth linear algebraic solvers are used to solve the symmetric matrix and asymmetric matrix, respectively. The

pressure-implicit with splitting of operators (PISO) algorithm was adopted to achieve the pressure-velocity coupling, which accelerates the convergence speed during the iterative process. More details about discretisation and coupled solve can be found in [32]. The initial and boundary conditions are specifically discussed in Section 3.2.

In addition, the roughness of the terrain surface in the ANSYS-CFX package is reflected by the roughness height. It depends on the geometry, size and arrangement of surface roughness elements. A technical roughness described by the equivalent sand-grain roughness is required as the input parameter.

2.2. Rheological Properties

Tailings slurry is a mixture of tailings and water. In the initial process of dam failure caused by overtopping, a mass of floodwater is discharged with tailings, so that the velocity of tailings is nearly equal to that of the water. Then a significant velocity discrepancy occurs between tailings and water, so that the tailings gradually deposit and separate from the flow. Consequently, the tailings flow becomes inhomogeneous, making it difficult to depict rheological properties. Thus, tailings flow is still treated as a homogeneous fluid throughout the whole evolution in many cases [33–36].

Homogeneous fluid mainly includes Newtonian fluid, Bingham fluid, expansible fluid, pseudoplastic fluid and yielding pseudoplastic fluid. Many researchers reported that Bingham fluid can represent tailings flow or debris in various situations [37–40]. For further discussion, the rheological properties of tailings slurry were measured through a rheometer in laboratory tests (Figure 1a). The specific gravity of the tailings (Gs) is 2.64, the average particle size (d_{50}) is 0.11 mm and the fine particles (0.075~0.25 mm) accounted for almost two-thirds of the tailings. The tailings sample from the lead-zine mine tailings site was mixed with water to form the slurry for experiments. Five groups of slurry were prepared with the mass concentration (C) of 60%, 65%, 70%, 75% and 80%. The experimental data scatter points and fitting curves are exhibited in Figure 1b. It can be observed that the rheological results of slurry conform to the Bingham model, which can be described as follow:

$$\tau = \tau_0 + \mu\gamma \tag{8}$$

where τ is the viscous shear stress, τ_0 is the yield shear stress, μ is the viscosity and γ is the shear rate. Yield shear stress and dynamic viscosity, the two rheology parameters of Bingham fluid, were the value of the intercept and slope of the line, respectively.
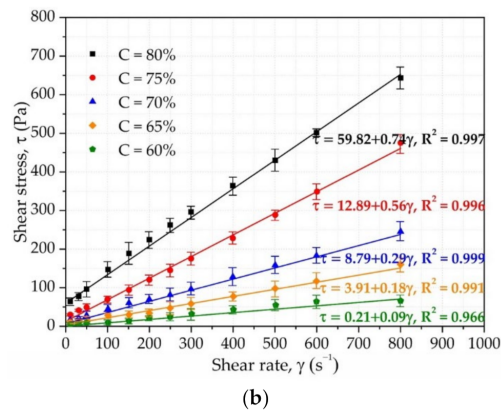

(a)

Figure 1. *Cont.*

(**b**)

Figure 1. Testing apparatus and rheological results of slurry: (**a**) Rheometer testing apparatus; (**b**) Shear stress and shear rate relationships with fitted curves.

3. CFD Simulation

3.1. Validation

The flume test of a non-Newtonian dam-break flow conducted by Minussi [41] was used for the validation. The specimen of Carbopol solution (Lubrizol, Wickliffe, OH, USA), a Herschel–Bulkley fluid, was prepared and filled in the reservoir. A vertical gate was pulled upward by a hydraulic piston to cause the dam failure. Then the fluid stored in the reservoir was released and began flow. A guide grid was positioned on the lateral acrylic wall. A JVC digital camera (GY DV 500) was set to take a sequence of snapshots of the flow movement.

The CFD method was applied to simulate the above experiment for validation. A geometric model with the identical size of the flume was established and meshed with structure grids. The initial reservoir high was chosen to be 0.1 m. The Herschel–Bulkley model is given by Equation (9)

$$\tau = \tau_0 + k\gamma^n \tag{9}$$

where τ_0 is the yield shear stress; k is the consistency, γ is the shear rate and n is the flow index. It is a generalised model of the Bingham model for $n = 1$.

The same rheological parameters from Minussi's experiments were used ($\tau_0 = 30.002$ Pa, $k = 4.297$ Pa $\times s^n$, $n = 0.479$). The gate influence was disregarded and the flow began due to the pressure difference. The Volume of Fluid (VOF) method was adopted to analyze the multiphase flow. The turbulent terms were analyzed through a first-order upwind scheme. The transient terms were approximated by a second-order implicit scheme.

Figure 2 exhibits the numerical and experimental comparison of the wave front horizontal positions [41]. As shown in Figure 2, all the curves display the same trend of wave front horizontal positions rapidly increasing at the beginning and gradually levelling off. It is worth noting that numerical results presented greater distances than the experimental results. One possible reason is that the experimental data were captured at the sidewall, rather than at the flow's centerline, leading to smaller values. In addition, lateral friction, gate influence and surface tension were disregarded in numerical simulations, contributing to the discrepancy. The numerical simulation in this study was consistent with experimental results for the use of complete motion equations of non-Newtonian fluid. Overall, the good agreement in this study between the calculated results and experimental results validates the applicability of the numerical method.
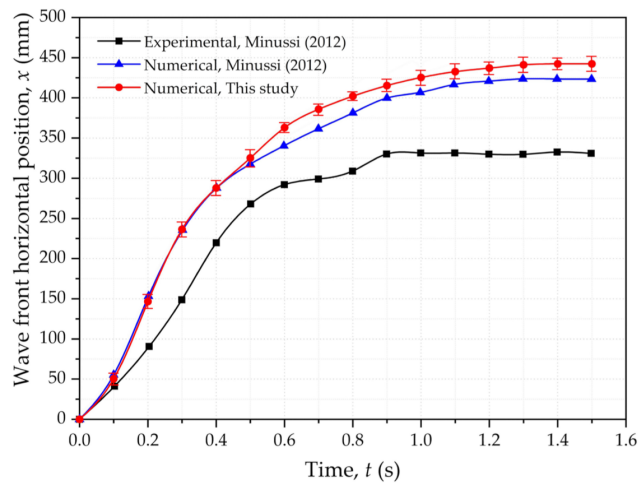
Figure 2. Numerical–experimental comparison of the wave front horizontal positions.

3.2. Dagangding Tailings Dam Failure

For exploring the variations in tailings flow characteristics against terrain features, a 3D simulation was carried out based on the topographic data of the Dagangding case.

The Dagangding tailings dam is located in Longkou Town, Heshan City, Guangdong Province, China, with 22°47′15″~22°50′23″N and 112°50′58″ to 112°53′28″E (Figure 3a). The region has a subtropical monsoon climate with an abundance of typhoons and rainstorms in summer and autumn. The average annual temperature is 22.6 °C, and the average precipitation is about 1700 mm.
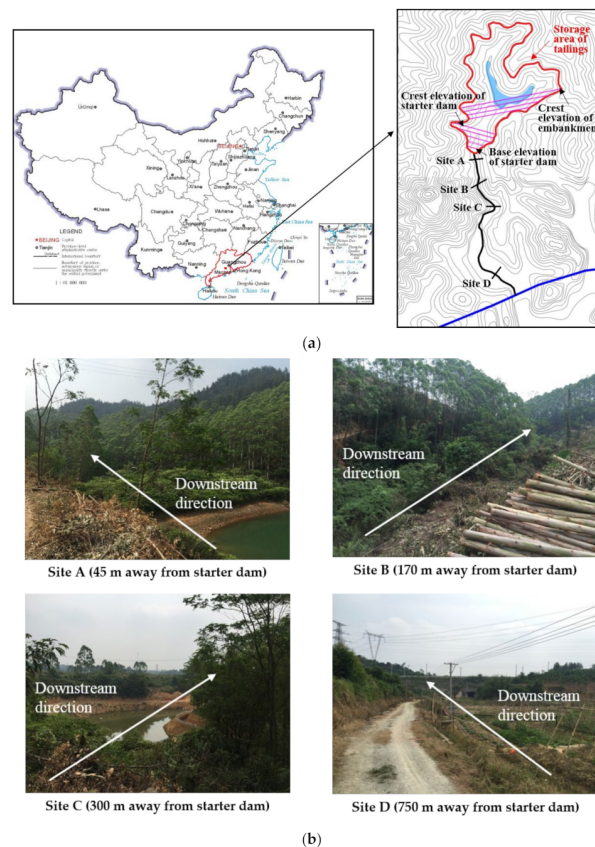

Figure 3. Location, topographic map, and downstream landforms of the Dagangding tailings dam: (**a**) Location and topographic map; (**b**) Landform of four typical sites.

The location and topographic map of the tailings dam can be seen in Figure 3a, and its characteristics are listed in Table 1. The tailings dam belongs to grade IV, and it was constructed by the upstream embankment method. Floods over a 200-year period were considered for flood control standards. The starter dam is a permeable rockfill dam about 17 m high, and the height of the embankment is 40 m. The Dagangding tailings dam has a total storage capacity of 358.86×10^4 m^3 and a catchment area of about 0.327 km^2. The downstream gully meanders through different landforms (Figure 3b). Site A and Site B abound with shrubs and trees, and the landform between them is narrow and straight. The landform flattens gradually from Site B to Site C. Significantly, an apparent turning of about 80° appears at site C. Across site C for approximately 200 m, a wide and flat grassland with farmland around site D appears. A railway is situated 850 m away, and behind it is a village with about three hundred people.

Table 1. Characteristics of the Dagangding tailings dam.

Concept	Contents or Values
Grade	IV
Construct method	Upstream embankment method
Flood control standard	Flood in a 200-year
Height of starter dam	17 m
Height of embankment	40 m
Whole storage capacity	358.86×10^4 m^3
Catchment area	0.327 km^2

The region from the dam breach to the railway was chosen as the calculation zone in the simulation. The erosion influence was out of scope in this paper. For characterising the actual terrain, the ground surface was interpolated from contour data of the topographic map through MIDAS-GTS software (version of 2013 R1). Then the geometric model was conducted and meshed in the ICEM software (version of 14.5) (Figure 4). Tetrahedral meshes were used in the majority area, with a maximum volume mesh size of 30 m^3 and a maximum face mesh size of 10 m^2. The pentahedral prism meshes were adopted near the boundary of the inlet and ground surface, with a maximum volume mesh size of 10 m^3 and a minimum volume mesh size of 2 m^3. The mesh consisted of 543,243 elements and its total number of nodes was 109,680. The Bingham model was considered for the case based on rheological results. The rheological values at a mass concentration of 70% were selected for a conservative estimation. Parameters in the numerical analysis are displayed in Table 2.
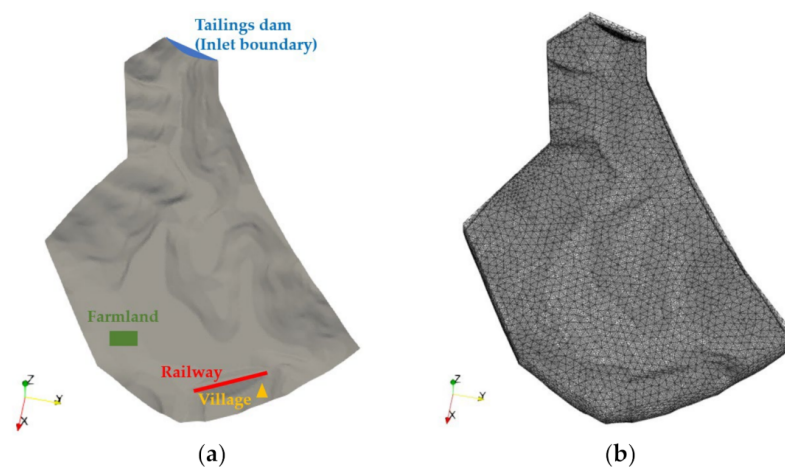

(a)   (b)

Figure 4. Diagram of the computational domain: (**a**) the geometric model; (**b**) the meshes.

Table 2. Parameters in numerical analysis.

Parameters	Values
Fluid density, ρ (g/cm^3)	1.82
Mass concentration, C (%)	70
Yield stress, τ_0 (Pa)	8.79
Viscosity, μ (Pa·s)	0.29

Since the process of breach development involved considerable uncertainty, it was assumed that the dam collapsed instantaneously, ignoring the dynamic hydrograph associated with the breach development. That is, the geometry of the breach (length, width and height) after dam-break was assumed to be constant.

Rather than the entire volume of the reservoir dam being discharged, some tailings remained in the tailings pond after dam failure. The quantitative assessment of potential consequences caused by tailings flow requires an appropriate estimation of the discharge volume of tailings slurry. A common conservative approach is to choose the deepest dam break section, which collapses along the residual friction angle of the starter dam. After calculating the deepest dam break section, it was concluded that the discharge volume of the tailings slurry was one third of the total storage capacity, with a value of 1.20×10^6 m^3. Then the breach width was calculated by the empirical equation [42] as below:

$$b = K\left(W^{\frac{1}{2}}B^{\frac{1}{2}}H\right)^{\frac{1}{2}} \tag{10}$$

where W is the discharge volume and equals 1.20×10^6 m^3; K is the empirical coefficient for the materials of starter dam and equals 0.65; B is the crest width and equals 497.7 m; H is the head of the dam-break and equals 57.0 m; calculating the breach width b equals 76.7 m.

The maximum discharge rate at breach (Q_m) has an important influence on the final inundation extent. On the basis of dam-break flood theory and debris flow correction [43], Q_m was calculated by:

$$\begin{cases} Q_m = (1+\varnothing)D_m Q_w \\ \varnothing = \frac{\rho-1}{G_s-\rho} \\ Q_w = 0.27\left(\frac{L}{B}\right)^{\frac{1}{10}}\left(\frac{B}{b}\right)^{\frac{1}{3}}\sqrt{g}b(K'h)^{\frac{3}{2}} \\ K' = 1.4\left(\frac{bhH_0}{B}\right)^{\frac{1}{3}} \end{cases} \tag{11}$$

where $\varnothing$ is the correction factor for tailings weight; ρ is the fluid density and equals 1.82 g/cm^3; G_s is the specific gravity of tailings and equals 2.64; D_m is the empirical coefficient for clogging of the drainage system and equals 1.5; L is the crest length and equals 375 m; K' is the empirical coefficient for dam geometry; h is the average height of residual after break, H_0 is water depth before the dam break and equals 5 m; calculating the maximum discharged rate of water at dam breach Q_w is 1312.9 m^3/s and then the maximum discharge rate at breach Q_m equals 3892.9 m^3/s.

According to the relationship between the instantaneous dam-break flow process, the maximum discharge rate at breach and the discharge volume, the flow process curve at breach is approximately simplified as a quaternary parabola [44] as below:

$$Q = Q_m\left(\frac{Q_m}{5W}t - 1\right)^4 \tag{12}$$

where Q is the discharge flow rate of tailings slurry at dam breach at the time t.

In this case, the hydrograph of tailings flow at dam breach is shown in Figure 5. The inlet boundary condition was set as bulk mass flow rate, obtained from the product of the discharge flow rate (Q) multiplied by the fluid density (ρ).
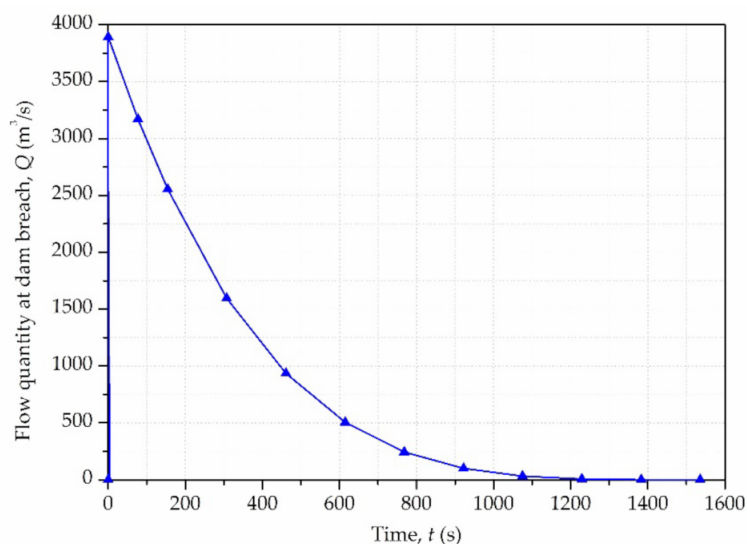

Figure 5. The hydrograph of tailings flow at dam breach.

The outlet and top surface were free boundaries. According to Davenport's classification of major shrub cover, the ground was set with a roughness height of 0.03 m. Surrounding surfaces used smooth wall boundaries.

It should be noted that different assumptions about the material model and boundary conditions result in distinct numerical results on runout distance, inundation area, etc. In this study, the tailings flow characteristics linking practical topographic features were investigated in a conservative scenario combining the simplified model, constant parameters and supernumerary influx.

4. Results and Discussion

4.1. Flow Velocity and Runout Distance

Flow velocity is an important index to evaluate the characteristics of tailings flow. As shown in Figure 6, the velocities of tailings flow decreased along the runout path. In the initial 10 s, the flow velocity increased rapidly, and the peak value of about 8 m/s was identified at the flow front (Figure 6a). After the peak velocity, it slowed down gradually due to energy dissipation from the friction and collision during the propagation (Figure 6b). Soon after, the difference between terrain and altitude enabled a velocity drop in the tailings flow (Figure 6c). Then a rapid decline in flow velocity was noted with a sharp turning (Figure 6d). After the deflection, the tailings flow underwent a decelerated process to 2.65 m/s (Figure 6e). At 320 s, the flow spread over the flat area where the farmland was located. At this stage, the front flow was approaching but had not crossed the railway (Figure 6f). Thereafter, the flow began to stabilise, moving slowly downstream, and divided into two branches (Figure 6g). Finally, the tailings flow stopped at t = 1280 s (about 22 min), with a runout distance of approximately 750 m (Figure 6h). It can be inferred that the village behind the railway would not be affected, as the volume and velocity of the tailings flow had reduced significantly.
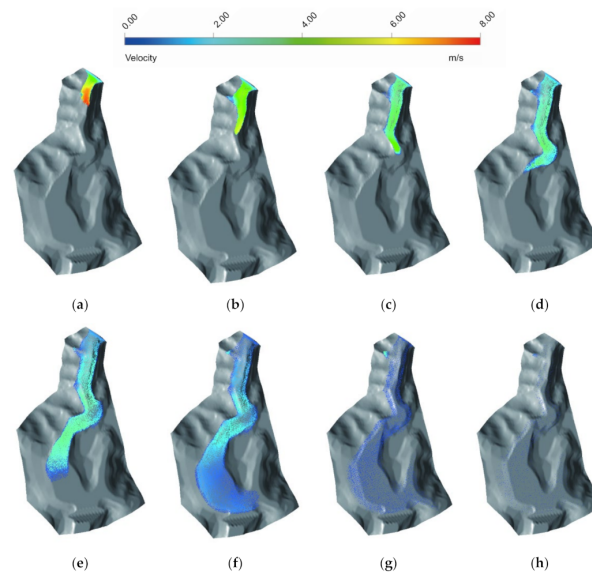
Figure 6. Velocity variations at different times for the process of the Dagangding tailings flow: (**a**) t = 10 s; (**b**) t = 20 s; (**c**) t = 40 s; (**d**) t = 80 s; (**e**) t = 160 s; (**f**) t = 320 s; (**g**) t = 640 s; (**h**) t = 1280 s.

To further investigate the characteristics of tailings flow, Figure 7 exhibits the time history curves of the flow distance and velocity. The blue curve represents the runout distance of the front flow, and the red curve indicates the velocity of the front flow. It took approximately 200 s for the front flow to reach most distances. Afterwards, the movement gradually stopped over 600 s. The runout distance was approximately 750 m. It can be noted that the velocity of front flow reached a peak velocity of about 8 m/s, and decreased rapidly to about 3 m/s during the initial 100 s. Then the velocity gradually dropped in the following 700 s, which conformed to the effect of flatter terrain. Eventually, the flow stopped at about 1280 s. In addition, it was observed that the time response of distance lagged behind that of velocity.
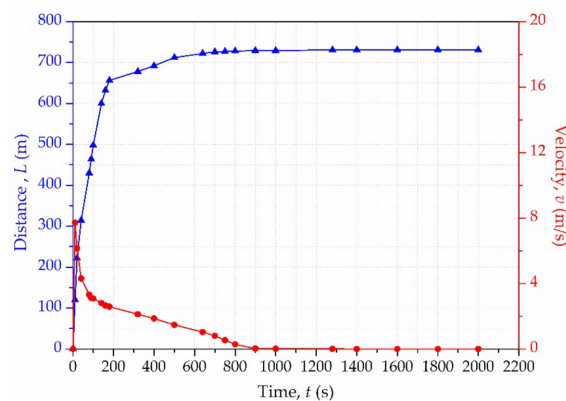

Figure 7. Distance and velocity of the front flow during the evolution process.

4.2. Inundation Area and Depth

The final inundation area and depth for the Dagangding tailings flow are presented in Figure 8. The elevation is shown in a colour band from light to dark green. The inundation area is represented by the grey colour. Furthermore, the inundation depth along the runout path is depicted in different shades of grey. It can be seen that most tailings were deposited near the dam breach, due to the gravity effect. The maximum inundation depth was 25.6 m. The inundation depth was greatly influenced by the variations in the downstream terrain. Tailings accumulated at sharp corners and spread out in flat areas, such as the farmland.
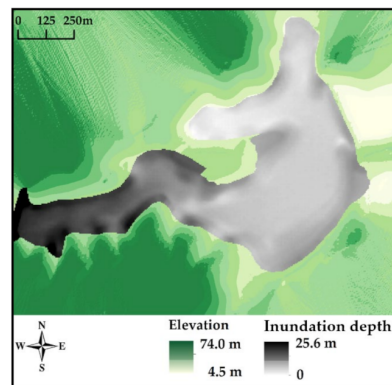
Figure 8. Inundation area and thickness for the process of the Dagangding tailings flow.

In addition, the final profile of the Dagangding tailings flow along the flow path is portrayed in Figure 9a. The black curve means the elevation of the original surface, and the red curve refers to that of the final surface. Furthermore, their difference represents the deposit of the tailings flow. This proves the decreasing trend of the inundation depth along the path. The deposition depends on both energy dissipation and the variation of terrain. The cross sections of four typical sites, associated with Site A, Site B, Site C and Site D in Figure 3, are shown in Figure 9b. Site A and Site B were located in the valley with an obvious elevation difference from the surrounding hills. Site C displayed the sharp turning of the flow path. Site D was relatively wide and flat near the farmland and had some power facilities. The average inundation depth remained relatively stable between Site A (15.8 m), Site B (14.3 m) and Site C (13.6 m), but reduced swiftly at Site D (0.8 m). When the front flow reached the furthest distance of about 750 m, the inundation depth was about 0.3 m. Since the railway was approximately 2 m above the original surface elevation, the village behind it would not be affected.
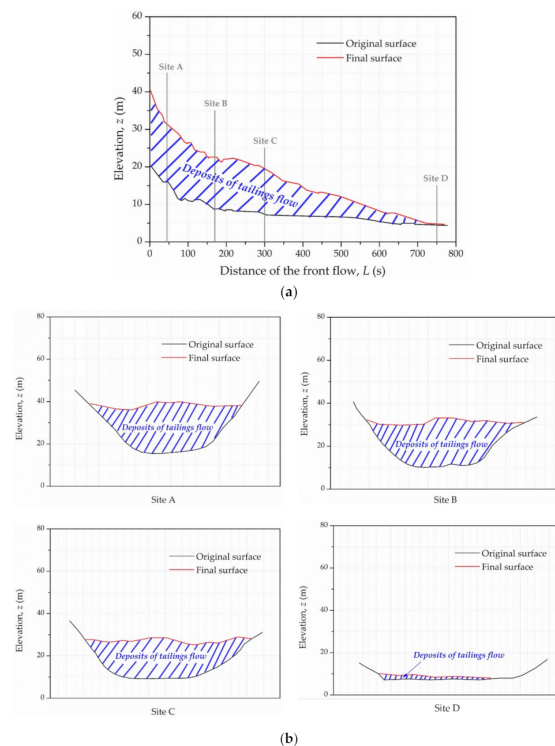

Figure 9. Numerical results of the Dagangding tailing flow: (**a**) final profile; (**b**) cross sections of four typical sites.

5. Protection and Control Measures

Tailings flow significantly impacts people's livelihood and the surrounding ecological environment. For this reason, engineers have proposed several control measures, such as setting a check dam and planting trees or grasses. To investigate the effects of the two measures, a simplified numerical model (Figure 10) was established. The starter dam and embankment heights were 20 m and 10 m, respectively. A regular rectangular channel was set measuring 500 m in length and 40 m in width. The rheological parameters were obtained from previous experiments at a mass concentration of 70%. The inlet mass flow rate at dam breach was calculated by Equation (9) with a released volume of $W = 5 \times 10^4 \text{ m}^3$.
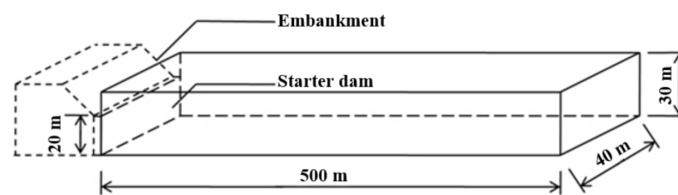

Figure 10. Simplified model of a tailings dam and the downstream channel.

5.1. Setting the Check Dam

Setting the check dam is essential for resisting the dynamic force of dam-break-type flows [45–48]. A gravity impermeable check dam with a trapezoid cross section was considered in numerical simulation. In order to evaluate its blocking effect with various locations and heights, six cases are summarised in Table 3. Case 1 (with no check dam) was used as the base case. Cases 2–6 were set at different locations (100 m, 200 m, 300 m) with various heights (2 m, 3 m, 4 m).

Table 3. Summaries of setting check dam in numerical simulation.

Name	Check Dam Location [1], L (m)	Height of the Check Dam, H (m)
Case 1 [2]	0	0
Case 2	100	3
Case 3	200	3
Case 4	300	3
Case 5	200	2
Case 6	200	4

[1] Location refers to the distance away from the starter dam; [2] Case 1 refers to the condition of no check dam.

As shown in Figure 11, the front flow distances shortened remarkably compared with the base case (Case 1). Additionally, the distance increased with increasing check dam locations. It is evident that distance reductions of 61% (Case 2), 35% (Case 3) and 13% (Case 4) occurred relative to the base case. However, the fluid level was raised before the check dam and then dropped quickly behind it. Furthermore, the maximum inundated thickness decreased with increasing check dam locations, which are 12.0 m, 6.2 m and 4.1 m of Case 2, Case 3 and Case 4, which are 12.0 m, 6.2 m and 4.1 m of Case 2, Case 3 and Case 4. Therefore, a suitable location is essential, neither too far away nor too close to the dam breach. In addition, it is noteworthy that similar curves appear for the check dam at the same location with different heights. Both the front flow distance and the inundation depth of three cases (Case 3, 5 and 6) presented quite closed values. Thus, the height was relatively unimportant when setting the check dam. It is concluded that a check dam can effectively intercept the tailings flow with proper design, consistent with the results of existing studies [28,48]. Unfortunately, a scenario involving multiple check dams is beyond the scope of this article.
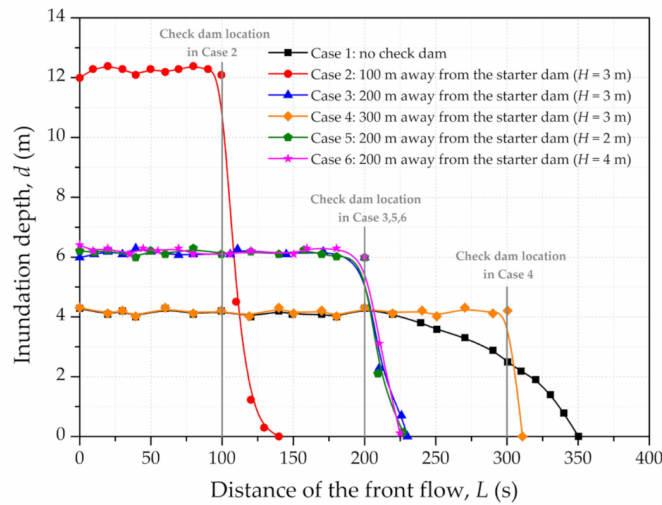
Figure 11. The inundation depth along the downstream channel.

5.2. Planting Trees or Grasses

Planting trees or grasses is a generally accepted measure for protecting against the tailings flow hazard [49,50]. Different types of plant cover have different surface roughnesses. The roughness length (Z_0) is used to describe the surface roughness in numerical simulation. The roughness length (Z_0), an aerodynamic term defined numerically as the height where the wind velocity is zero (it does not exist physically), reveals the roughness characteristics of the terrain [51]. It is generally independent of airflow and only depends on the geometry, size and arrangement of surface roughness elements. It is difficult to obtain real values of the surface roughness under heterogeneous conditions, therefore, practical estimation is often based on published values for roughness of similar terrain elsewhere [52]. Since Davenport's classification of effective terrain roughness has proven to be reliable [51,52], four typical classes (Class 3, Class 4, Class 6 and Class 7) in the classification were selected to represent four types of plant cover (Type 1, Type 2, Type 3 and Type 4), as shown in Table 4.

Table 4. Summaries of roughness length.

Classes	Roughness Length, Z_0 (m)	Types of Plant Cover
Class 1. Sea	0.0002	\
Class 2. Smooth	0.005	\
Class 3. Open	0.03	Type 1. Grasses cover
Class 4. Roughly open	0.10	Type 2. Low crops cover
Class 5. Rough	0.25	\
Class 6. Very rough	0.5	Type 3. Shrubs cover
Class 7. Skimming	1.0	Type 4. Trees cover
Class 8. Chaotic	$\geq$2.0	\

Figure 12 shows the distance–time history curves of different types of plant cover. It is evident that the variation trend is similar. The front flow distance increases rapidly in the initial 200 s, and a gradual decline in velocity is noted with the slow-growing distance. Planting trees or grasses can shorten the runout distance while protecting the ecological environment. Moreover, the runout distance reduces with an increase in the roughness length. Taking Type 1 (grass cover) and Type 4 (tree cover) for comparison, it can be seen that the runout distance of Type 4 reduces by 32.02% compared with that of Type 1. Therefore, the type of plant cover plays an important role in mitigating the impact of tailings flow. In addition, the specific implementation should be carried out according to local conditions, such as terrain, slope, soil thickness and others.
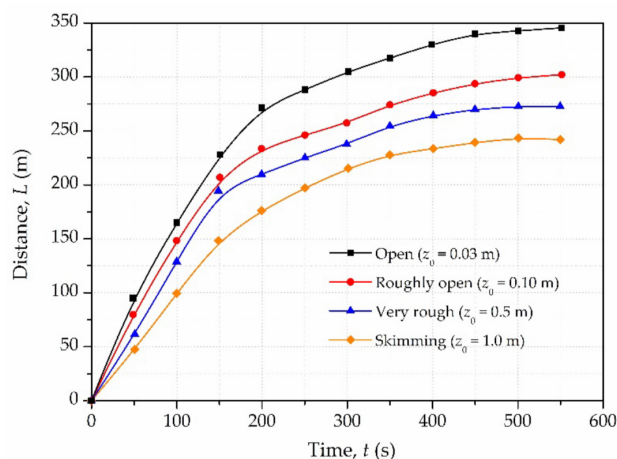
Figure 12. Distance–time history curves of different types of plant cover.

6. Conclusions

Tailings flow from dam breaks represent a complex problem of physical mechanics and fluid properties. In this paper, tailings flow is assumed to be an incompressible non-Newtonian fluid following the Navier–Stokes governing equations. The rheological properties of tailings slurry with different mass concentrations were studied by laboratory experiments. Subsequently, the results were further used in a numerical simulation. The method was validated with flume experiments of a non-Newtonian dam-break flow with good consistency. A framework combining the three-dimensional CFD model with complex terrain reconstruction was established to dig into the mechanism of the tailings flow. Finally, protection and control measures for potential tailings flow hazards were discussed. The following conclusions can be drawn:

(1) The experimental results signify that this tailings slurry, composed of lead-zine mine tailings with about two-thirds fine particles (0.075~0.25 mm), conformed to the Bingham model. The two rheological parameters of the Bingham model, yield shear stress and dynamic viscosity, were obtained. A non-linear relationship between the mass concentration and yield shear stress or dynamic viscosity was observed.

(2) The variation in flow characteristics (flow velocity, runout distance, inundation area and depth) against the terrain features in the Dagangding case were analyzed within our framework. Results show that a sharp turning can bring in a rapid decline in flow velocity, implying a flow regime transition. Varying roughness can make a difference when referring to the runout distance. The runout distance and the roughness form a negative relationship. A similar relationship can be also seen between inundation depth and sudden flattening. A decrease in sudden flattening contributes to higher aggregation of the tailings. Meanwhile, the flow lasted about 1280 s (about 22 min), possessing a maximal runout distance of about 750 m, which shows that the downstream railway and concerned villages would not be affected in a conservative scenario.

(3) The effects of protective measures, including setting a check dam and planting trees or grasses on the tailings flow, were studied. The development of the tailings flow can be effectively constrained by a properly designed check dam. Its location, rather than its height, plays a dominant role in blocking the flow. In addition, planting trees or grasses can shorten the runout distance while protecting the ecological environment. in this study, the types of plant cover influenced the runout distance of the tailings flow, and the distance of Type 4 (tree cover) was less than (reduced by 32.02%) that of Type 1 (grass cover).

Even though the proposed numerical framework is beneficial for investigating the tailings flow, there also remain some limitations. In this research, the material model was assumed to be isotropic and incompressible, and the mechanical behaviour conformed to

an ideal Bingham model. Some state variables (fluid density and mass concentration) were time-independent and may have introduced computational errors. The authors intend to add the optimisation of the material model to their future work. Moreover, the boundary condition can be seen as another aspect of the methodology to be improved. The current iteration scheme experienced difficulty in mimicking the influx for the inlet boundary condition. It seemed to be unable to accurately characterise the breach development, discharge volume and discharge flow rate along with time up to date. For this reason, the authors made some assumptions to compensate, for example by calculating the discharge volume from the deepest dam break section. Such a conservative condition may overestimate the total flux. From a future perspective, the authors plan to introduce more failure criteria for a concise discharging volume calculation. The final point concerns the roughness setting of the ground. Uniform roughness was assumed herein, but a grid-wise distribution of the roughness can be adopted in the future. In summary, the authors believe the major factors for further improvement are the variation in material properties, the dam breach process and the refinement of the ground condition.

Author Contributions: Conceptualization, Y.Y. and X.Z.; methodology, Y.Y.; software, Y.Y. and X.C.; validation, Y.Y., X.Z. and C.X.; formal analysis, Y.Y. and X.C.; investigation, Y.Y.; resources, X.Z.; data curation, Y.Y and X.C.; writing—original draft preparation, Y.Y.; writing—review and editing, C.X.; visualization, Y.Y.; supervision, X.Z. All authors have read and agreed to the published version of the manuscript.

References

1. Kossoff, D.; Dubbin, W.E.; Alfredsson, M.; Edwards, S.J.; Macklin, M.G.; Hudson-Edwards, K.A. Mine tailings dams: Characteristics, failure, environmental impacts, and remediation. *Appl. Geochem.* **2014**, *51*, 229–245. [CrossRef]
2. Parbhakar-Fox, A.; Glen, J.; Raimondo, B. A Geometallurgical Approach to Tailings Management: An Example from the Savage River Fe-Ore Mine, Western Tasmania. *Minerals* **2018**, *8*, 454. [CrossRef]
3. Chronology of Major Tailings Dam Failures, World Information Service on Energy. Available online: https://www.wise-uranium.org/mdaf.html (accessed on 21 December 2021).
4. International Commission on Large Dams (ICOLD); United Nations Environmental Programme (UNEP). *Tailings Dams-Risk of Dangerous Occurrences, Lessons Learnt from Practical Experiences (Bulletin 121)*; International Commission on Large Dams: Paris, France, 2001.
5. Rico, M.; Benito, G.; Salgueiro, A.R.; Diez-Herrero, A.; Pereira, H.G. Reported tailings dam failures: A review of the European incidents in the worldwide context. *J. Hazard. Mater.* **2008**, *152*, 846–852. [CrossRef] [PubMed]
6. Shahid, A.; Qiren, L. Tailings dam failure: A review of the last one hundred years. *Geotech. News* **2010**, *28*, 50–53.
7. Santamarina, J.C.; Torres-Cruz, L.A.; Barchus, R.C. Why coal ash and tailings dam disasters occur. *Science* **2019**, *364*, 526–528. [CrossRef]
8. Zhang, L. Summary on the dam-break of tailing pond. *J. Hydraul. Eng.* **2013**, *44*, 594–600. (In Chinese)
9. Wei, Z.; Yin, G.; Wang, J.G.; Wan, L.; Li, G. Design, construction and management of tailings storage facilities for surface disposal in China: Case studies of failures. *Waste Manag. Res.* **2013**, *31*, 106–112. [CrossRef]
10. Yu, G.; Song, C.; Pan, Y.; Li, L. Review of new progress in tailing dam safety in foreign research and current state with development trend in China. *Chin. J. Rock Mech. Eng.* **2014**, *33*, 3238–3248. (In Chinese)
11. Peng, K.; Zhou, J.; Zou, Q.; Zhang, J.; Wu, F. Effects of stress lower limit during cyclic loading and unloading on deformation characteristics of sandstones. *Constr. Build. Mater.* **2019**, *217*, 202–215. [CrossRef]
12. Pastor, M.; Martin Stickle, M.; Dutto, P.; Mira, P.; Fernández Merodo, J.A.; Blanc, T.; Sancho, S.; Benítez, A.S. A Viscoplastic Approach to the Behaviour of Fluidized Geomaterials with Application to Fast Landslides. *Contin. Mech. Thermodyn.* **2013**, *27*, 21–47. [CrossRef]

13. Ghahramani, N.; Mitchell, A.; Rana, N.M.; Mcdougall, S.; Evans, S.G. Tailings-Flow Runout Analysis: Examining the Applicability of a Semi-Physical Area-Volume Relationship Using a Novel Database. *Nat. Hazards Earth Syst. Sci.* **2020**, *7*, 1–23. [CrossRef]

14. Larrauri, P.C.; Lall, U. Tailings dams failures: Updated statistical model for discharge volume and runout. *Environments* **2018**, *5*, 28. [CrossRef]

15. Alhasan, Z.; Jandora, J.; Riha, J. Comparison of specific sediment transport rates obtained from empirical formulae and dam breaching experiments. *Environ. Fluid Mech.* **2016**, *16*, 1–23. [CrossRef]

16. Börzsönyi, T.; Ecke, R.E.; McElwaine, J.N. Patterns in flowing sand: Understanding the physics of granular flow. *Phys. Rev. Lett.* **2009**, *103*, 1–4. [CrossRef] [PubMed]

17. Wu, T.; Qin, J. Experimental Study of a Tailings Impoundment Dam Failure Due to Overtopping. *Mine Water Environ.* **2018**, *37*, 272–280. (In Chinese) [CrossRef]

18. Chraml, K.; Thomschitz, B.; McArdell, B.W.; Graf, C.; Kaitna, R. Modeling debris-flow runout patterns on two alpine fans with different dynamic simulation models. *Nat. Hazards Earth Syst. Sci.* **2015**, *15*, 1483–1492. [CrossRef]

19. Yoon, J.J.; Shim, J.S.; Park, K.S.; Lee, J.C. Numerical experiments of storm winds, surges, and waves on the south- ern coast of Korea during Typhoon Sanba: The role of revising wind force. *Nat. Hazards Earth Syst. Sci.* **2014**, *14*, 3279–3295. [CrossRef]

20. Mizani, S.; He, X.; Simms, P. Application of lubrication theory to modeling stack geometry of high density mine tailings. *J. Non-Newton. Fluid Mech.* **2013**, *198*, 59–70. [CrossRef]

21. Henriquez, J.; Simms, P. Dynamic imaging and modelling of multilayer deposition of gold paste tailings. *Miner. Eng.* **2009**, *22*, 128–139. [CrossRef]

22. Jing, X.; Chen, Y.; Xie, D.; Williams, D.J.; Wu, S.; Wang, W.; Yin, T. The Effect of Grain Size on the Hydrodynamics of Mudflow Surge from a Tailings Dam-Break. *Appl. Sci.* **2019**, *9*, 2474. [CrossRef]

23. Iverson, R.M. Scaling and design of landslide and debris-flow experiments. *Geomorphology* **2015**, *244*, 9–20. [CrossRef]

24. Pastor, M.; Quecedo, M.; Merodo, J.A.F.; Herrores, M.I.; Gonzalez, E.; Mira, P. Modelling Tailings Dams and Mine Waste Dumps Failures. *Géotechnique* **2002**, *52*, 579–591. [CrossRef]

25. Dutto, P.; Stickle, M.M.; Pastor, M.; Manzanal, D.; Yague, A.; Tayyebi, S.M.; Lin, C.; Elizalde, M.D. Modelling of Fluidised Geomaterials: The Case of the Aberfan and the Gypsum Tailings Impoundment Flowslides. *Materials* **2017**, *10*, 562. [CrossRef] [PubMed]

26. Babaoglu, Y.; Simms, P.H. Simulating Deposition of High Density Tailings Using Smoothed Particle Hydrodynamics. *Korea-Aust. Rheol. J.* **2017**, *29*, 229–237. [CrossRef]

27. Wang, G.; Tian, S.; Hu, B.; Xu, Z.; Chen, J.; Kong, X. Evolution Pattern of Tailings Flow from Dam Failure and the Buffering Effect of Debris Blocking Dams. *Water* **2019**, *11*, 2388. [CrossRef]

28. Wang, K.; Yang, P.; Hudson-Edwards, K.A.; Lyu, W.; Yang, C.; Jing, X. Integration of DSM and SPH to Model Tailings Dam Failure Run-Out Slurry Routing Across 3D Real Terrain. *Water* **2018**, *10*, 1087. [CrossRef]

29. Marsooli, R.; Wu, W. 3-D finite-volume model of dam-break flow over uneven beds based on VOF method. *Adv. Water Resour.* **2014**, *70*, 104–117. [CrossRef]

30. Pirulli, M.; Barbero, M.; Marchelli, M.; Scavia, C. The Failure of the Stava Valley Tailings Dams (Northern Italy): Numerical Analysis of the Flow Dynamics and Rheological Properties. *Geoenviron. Disasters* **2017**, *4*, 2–15. [CrossRef]

31. Yu, D.; Tang, L.; Chen, C. Three-Dimensional Numerical Simulation of Mud Flow from a Tailing Dam Failure across Complex Terrain. *Nat. Hazards Earth Syst. Sci.* **2020**, *20*, 727–741. [CrossRef]

32. ANSYS Inc. *ANSYS CFX-Solver Theory Guide, Version 14.5*; ANSYS Inc.: Canonsburg, PA, USA, 2011.

33. O'Brien, J.S.; Julien, P.Y. Physical properties and mechanics of hyperconcentrated sediment flows. In Proceedings of the Specialty Conference on Delineation of Landslide, Flash Flood and Debris Flow Hazard in Utah, Logan, UT, USA, 14–15 June 1985.

34. Launder, B.E.; Spalding, D.B. The numerical computation of turbulent flows. *Comput. Methods Appl. Mech. Eng.* **1974**, *3*, 269–289. [CrossRef]

35. Gao, J.; Fourie, A. Studies on thickened tailings deposition in flume tests using the computational fluid dynamics (CFD) method. *Can. Geotech. J.* **2019**, *56*, 249–262. [CrossRef]

36. Kwak, M.; James, D.F.; Klein, K.A. Flow behaviour of tailings paste for surface disposal. *Int. J. Miner. Process.* **2005**, *77*, 139–153. [CrossRef]

37. Jeyapalan, J.K.; Duncan, J.M.; Seed, H.B. Investigation of Flow Failures of Tailings Dams. *J. Geotech. Eng.* **1983**, *109*, 172–189. [CrossRef]

38. Luna, B.Q.; Remaître, A.; Van Asch, T.W.; Malet, J.P.; Van Westen, C.J. Analysis of debris flow behavior with a one dimensional run-out model incorporating entrainment. *Eng. Geol.* **2012**, *128*, 63–75. [CrossRef]

39. Jeong, S.W. The viscosity of fine-grained sediments: A comparison of low-to medium-activity and high-activity clays. *Engineering* **2012**, *154*, 1–5. [CrossRef]

40. Bisantino, T.; Fischer, P.; Gentile, F. Rheological characteristics of debris-flow material in South-Gargano watersheds. *Nat. Hazards* **2009**, *54*, 209–223. [CrossRef]

41. Minussi, R.B.; Maciel, G.d.F. Numerical Experimental Comparison of Dam Break Flows with Non-Newtonian Fluids. *J. Braz. Soc. Mech. Sci. Eng.* **2012**, *34*, 167–178. [CrossRef]

42. Chen, S.; Zhong, Q.; Ren, Q. Numerical model study on break development due to overtopping failure for earth-rock dam. *Hydro-Sci. Eng.* **2009**, *4*, 53–58. (In Chinese)

43. Guo, C.; Tang, Z. Study on the tailings dam-break model. *J. Saf. Sci. Technol.* **2010**, *6*, 63–67. (In Chinese)
44. Shi, H.; Liu, Z. Review and progress of research in numerical simulation of dam-break water flow. *Adv. Water Sci.* **2006**, *17*, 129–135. (In Chinese)
45. Shieh, C.L.; Guh, Y.R.; Wang, S.Q. The application of range of variability approach to the assessment of a check dam on riverine habitat alteration. *Environ. Geol.* **2007**, *52*, 427–435. [CrossRef]
46. Mizuyama, T. Structural countermeasures for debris flow disasters. *Int. J. Eros. Control Eng.* **2008**, *1*, 38–43. [CrossRef]
47. Liu, F.Z.; Xu, Q.; Dong, X.J.; Yu, B.; Frost, J.D.; Li, H.J. Design and performance of a novel multi-function debris flow mitigation system in Wenjia Gully, Sichuan. *Landslides* **2017**, *14*, 2089–2104. [CrossRef]
48. Chen, H.; Li, J.; Feng, S.; Gao, H.; Zhang, D. Simulation of Interactions between Debris Flow and Check Dams on Three-Dimensional Terrain. *Eng. Geol.* **2019**, *251*, 48–62. [CrossRef]
49. Wieringa, J. Representative roughness parameters for homogeneous terrain. *Bound. Layer Meteorol.* **1993**, *63*, 323–363. [CrossRef]
50. Schoenberger, E. Environmentally Sustainable Mining: The Case of Tailings Storage Facilities. *Resour. Policy* **2016**, *49*, 119–128. [CrossRef]
51. Davenport, A. Rationale for determining design wind velocities. *Proc. Am. Soc. Civ. Eng. J. Eng. Mech. Div.* **1960**, *86*, 39–68. [CrossRef]
52. Wieringa, J.; Davenport, A.; Grimmond, C.S.B.; Oke, T.R. New revision of Davenport roughness classification. In Proceedings of the 3rd European and African Conference on Wind Engineering, Eindoven, The Netherlands, 2–6 July 2001.